Electrifying $Ba_{0.5}Sr_{0.5}Co_{0.8}Fe_{0.2}O_{3−\delta}$ for focalized heating in oxygen transport membranes

Marwan Laqdiem, Julio García-Fayos, Laura Almar, Alfonso J. Carrillo, Álvaro Represa, José M. López Nieto, Sonia Escolástico, David Catalán-Martinez, Jose M. Serra *

Instituto de Tecnología Química (Universitat Politècnica de València–Consejo Superior de Investigaciones Científicas), Av. Los Naranjos s/n, E-46022 Valencia, Spain

ARTICLE INFO

ABSTRACT

Industry decarbonization requires the development of highly efficient and flexible technologies relying on renewable energy resources, especially biomass and solar/wind electricity. In the case of pure oxygen production, oxygen transport membranes (OTMs) appear as an alternative technology for the cryogenic distillation of air, the industrially-established process of producing oxygen. Moreover, OTMs could provide oxygen from different sources (air, water, CO_2, etc.), and they are more flexible in adapting to current processes, producing oxygen at 700–1000 °C. Furthermore, OTMs can be integrated into catalytic membrane reactors, providing new pathways for different processes. The first part of this study was focused on electrification on a traditional OTM material ($Ba_{0.5}Sr_{0.5}Co_{0.8}Fe_{0.2}O_{3−\delta}$), imposing different electric currents/voltages along a capillary membrane. Thanks to the emerging Joule effect, the membrane-surface temperature and the associated O_2 permeation flux could be adjusted. Here, the OTM is electrically and locally heated and reaches 900 °C on the surface, whereas the surrounding of the membrane was maintained at 650 °C. The O_2 permeation flux reached for the electrified membranes was ∼3.7 NmL min^{-1} cm^{-2}, corresponding to the flux obtained with an OTM non-electrified at 900 °C. The influence of depositing a porous $Ce_{0.8}Tb_{0.2}O_{2−\delta}$ catalytic/protective layer on the outer membrane surface revealed that lower surface temperatures (830 °C) were detected at the same imposed electric power. Finally, the electrification concept was demonstrated in a catalytic membrane reactor (CMR) where the oxidative dehydrogenation of ethane (ODHE) was carried out. ODHE reaction is very sensitive to temperature, and here, we demonstrate an improvement of the ethylene yield by reaching moderate temperatures in the reaction chamber while the O_2 injection into the reaction can be easily fine-tuned.
© 2023 Science Press and Dalian Institute of Chemical Physics, Chinese Academy of Sciences. Published by ELSEVIER B.V. and Science Press This is an open access article under the CC BY license (http://creativecommons.org/licenses/by/4.0/).

1. Introduction

The decarbonization of the industry has become an important strategy to transition to a safe climatic future [1,2]. Developing highly efficient and sustainable new chemical production routes is essential to decrease the carbon footprint of actual processes. Oxidative and selective reactions using pure oxygen, like CO_2-capture-enabling oxycombustion or oxidative dehydrogenation of paraffins, have been extensively studied [3–7]. In this matter, oxygen production will take an important role, and it is essential to develop new technologies that are more efficient and flexible to achieve these new challenges [3,8–11].
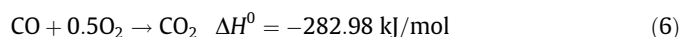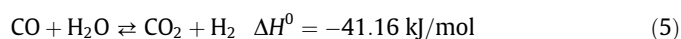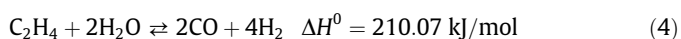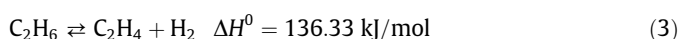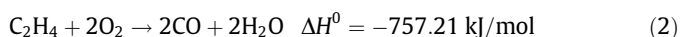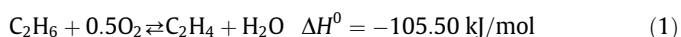
The current and most mature technology that provides pure oxygen (with production rates of up to 30,000 Nm^3 h^{-1} with 99% purity) is the cryogenic distillation of air. The economic sustainability of this technology relies on using large equipment and cryogenic conditions entailing high pressures [11]. Oxygen transport membrane (OTM) emerges as an alternative technology to produce pure oxygen, with more than 99.99% purity, more flexibility, and reduced costs [4,12]. In addition, this technology typically works at 700–1000 °C, allowing it to be integrated into current industrial processes presenting residual heat streams [13,14]. From a techno-economic point of view, the OTM must permeate 10 NmL min^{-1}-cm^{-2} of oxygen to be competitive with actual technologies [14]. However, the membranes that could achieve these permeability values are usually unstable or lose much activity when exposed to CO_2 environments [4,12]. $Ba_{0.5}Sr_{0.5}Co_{0.8}Fe_{0.2}O_{3−\delta}$ (BSCF)-based membranes could achieve high oxygen permeation values,

reaching more than 60 NmL min^{-1} cm^{-2} of O$_2$ [15–19]. This could lead to the use of this technology to produce pure oxygen [17]. However, in order to achieve that oxygen permeation, the membrane temperature must be around 900 °C, whereas these operating temperatures imply high equipment and operational costs.

BSCF membranes have been studied as catalytic membrane reactors for several relevant reactions to produce hydrocarbon fuels and chemicals [6,20–24], such as oxygen coupling of methane (OCM), partial oxidation of methane (POM), water splitting, oxidative dehydrogenation of ethane (ODHE), etc. ODHE technology has gained industrial interest, driven by the increasing global ethylene demand (precursor of polyethylene, ethylene oxide, and ethylbenzene), with expectations of ethylene production reaching almost 200 megatons by 2026 [25]. Currently, worldwide ethylene production comes from other sources like methane, naphtha, liquefied petroleum gas, etc. In fact, the steam cracking of naphtha represents more than 40% of the ethylene production [26]. From ethane feedstock, the main ethylene production route is the thermal cracking of ethane, achieving yields close to 60% and 70% [5]. Even so, thermal cracking has several issues regarding the deactivation through coke formation and the necessity of high operation temperatures (800–900 °C) [25]. Nevertheless, new technologies like protonic ceramic cells are being studied for the thermal cracking of ethane, displacing the equilibrium at lower temperatures [27–29]. Another approach is ODHE, which could be an alternative to this process, Eq. (1). In the ODHE process, the coke formation is reduced thanks to the presence of oxygen, and it can be realized in a broad temperature range (300–900 °C) [6,7,25,30–33]. These advantages make this technology a more efficient and sustainable process with potential for industrial deployment. However, several secondary reactions can occur in the presence of oxygen and at higher temperatures, decreasing the ethylene yield in the global process, Eqs. (2)–(6) [34].

$$C_2H_6 + 0.5O_2 \rightleftharpoons C_2H_4 + H_2O \quad \Delta H^0 = -105.50 \text{ kJ/mol} \tag{1}$$

$$C_2H_4 + 2O_2 \rightarrow 2CO + 2H_2O \quad \Delta H^0 = -757.21 \text{ kJ/mol} \tag{2}$$

$$C_2H_6 \rightleftharpoons C_2H_4 + H_2 \quad \Delta H^0 = 136.33 \text{ kJ/mol} \tag{3}$$

$$C_2H_4 + 2H_2O \rightleftharpoons 2CO + 4H_2 \quad \Delta H^0 = 210.07 \text{ kJ/mol} \tag{4}$$

$$CO + H_2O \rightleftharpoons CO_2 + H_2 \quad \Delta H^0 = -41.16 \text{ kJ/mol} \tag{5}$$

$$CO + 0.5O_2 \rightarrow CO_2 \quad \Delta H^0 = -282.98 \text{ kJ/mol} \tag{6}$$

When oxygen is supplied to the ethane dehydrogenation reaction, controlling the O$_2$/C$_2$H$_6$ ratio is essential to avoid a secondary reaction [6,25]. For fixed bed reactors, the oxygen is co-fed with the ethane, leading to several secondary reactions, reducing the ethylene selectivity (Fig. 1a) while the inlet O$_2$/C$_2$H$_6$ ratio is maintained out of flammability/explosion limits. Several chemical-looping technologies have been developed to reduce the inlet O$_2$/C$_2$H$_6$ ratio, where the redox catalyst in situ releases the oxygen (Fig. 1b) [25,30,35]. Here, a promising alternative to control the O$_2$/C$_2$H$_6$ is an integrated membrane reactor based on mixed ionic and electronic conductors (MIEC) to control oxygen injection along the reaction chamber (Fig. 1c) [6,36–38]. In both catalytic membrane reactors (CMRs) based on OTM and chemical looping reactor, the addition of oxygen is highly distributed, achieving low ratios of O$_2$/C$_2$H$_6$. OTMs are made of ceramic MIEC materials, and the oxygen permeation increases exponentially with temperature, reaching optimal permeation values at high temperatures, around 800 and 900 °C [6,37,38]. As mentioned before, ODHE reaction improves the selectivity of ethylene at low temperatures, so decreasing the reactor temperature in CMRs could be the key to enhancing the selectivity of ethylene for OTM as catalytic membrane reactors in ODHE reaction.

This study focuses on the electrification of OTMs to heat the membrane surface locally and maintain an intermediate temperature in the reactor chamber. As mentioned before, the main property of OTMs is their mixed ionic and electronic conductivity [4,15]. BSCF (MIEC material selected for this study) shows a total conductivity of 30 S cm^{-1} in air at 650 °C [39–41]. Applying a voltage difference on a BSCF sample leads to the appearance of an electric current that dissipates energy in the form of heat, commonly known as the Joule effect. This increase in the membrane temperature gives rise to the increased oxygen permeation while maintaining the reactor chamber at lower temperatures. Here, the surface-membrane temperature was controlled (up to 900 °C) by applying different voltages, regulating the oxygen permeation flux, while the reactor chamber was preserved at a lower temperature, e.g., 650 °C. Further, the study shows that the new operation regime enabled by the developed electrified-BSCF membrane reac-
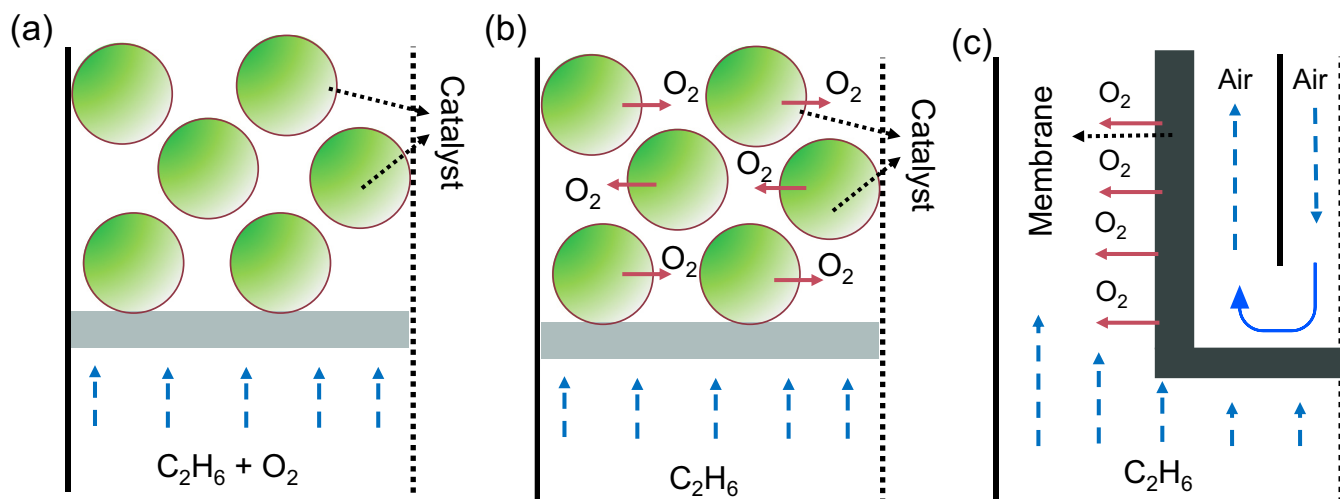

Fig. 1. Oxidative dehydrogenation of ethane reactors by using different modes of O$_2$ addition. (a) Co-feeding of oxygen and C$_2$H$_6$ in a fixed bed reactor; (b) feeding oxygen through the reduction of the catalyst in a chemical looping reactor; (c) feeding oxygen through an OTM in a catalytic membrane reactor.

tor ameliorates the catalytic ODHE performance, reaching higher ethylene yield than the non-electrified CMR.

2. Experimental

2.1. Material synthesis and membrane fabrication

For this study, commercial $Ba_{0.5}Sr_{0.5}Co_{0.8}Fe_{0.2}O_{3-\delta}$ (BSCF) capillaries from IKTS (Fraunhofer, Germany) were used with a length of 20 cm, an external diameter of 3 mm, and a thickness of 0.3 mm.

Two different catalytic layers were coated on BSCF capillaries, BSCF and $Ce_{0.8}Tb_{0.2}O_{2-\delta}$ (CTO). BSCF powder was provided by IKTS Fraunhofer (Germany), and CTO was synthesized using the Pechini method. Stoichiometric amounts of $Ce(NO_3)_3 \cdot 6H_2O$ (99.5% purity) and $Tb(NO_3)_3 \cdot 6H_2O$ (99.9% purity) provided by Sigma Aldrich were dissolved in a homogeneous aqueous solution. Afterward, citric acid (Sigma Aldrich) was added as a chelating agent to prevent partial segregation of metal components, and ethylene glycol (ThermoScientific) to polymerize with the chelating agent, producing an organometallic polymer (in a molar ratio 1:2:4, respectively). This complexation was followed by dehydration at 220 °C and thermal treatment at 850 °C for 5 h to form the desired fluorite phases.

The deposition of the catalytic layer was made by the dip-coating technique. Dip-coating inks were prepared using a three-roll mill, mixing 1:1 ceramic powder (BSCF or CTO) and vehicle Zvar (Zschimmer & Schwarz). Then, BSCF membranes were introduced into the ink for 5 s and extracted at a controlled speed. After each deposition, membranes were dried in two steps to ensure the catalytic layer was completely dried: first for 3 h at room temperature and finally for 2 h at 60–80 °C. After two dip-coating steps, membranes were heat-treated at 950 °C for 2 h. This coating provides an active surface of 3.01 cm^2 for the BSCF catalytic layer and 3.23 cm^2 for CTO catalytic layer, and the active length corresponds with the isothermal length of the reactor. To prevent oxygen permeation in the area without a catalytic layer, the membranes were covered with gold paper and then calcinated at 900 °C for 2 h.

2.2. Material characterization

Crystalline phases of the studied samples were identified using a PANalytical Cubix fast diffractometer, Cu K_α radiation (λ_1 = 1.54 06 Å), and an X'Celerator detector in Bragg-Brentano geometry. X-ray diffraction (XRD) patterns recorded in the 2θ range from 20° to 90° were analyzed using X'Pert Highscore Plus software. Cross-section analyses of the sintered materials before and after tests were conducted employing Field Emission Scanning Electron Microscopy (FESEM) in a ZEISS ULTRA 55. In addition, a backscattered electron detector (BSD) was used to provide images with compositional contrast that differentiate grains and element distribution.

2.3. Thermodynamic calculations

Thermodynamic simulations were performed using the software package HSC Chemistry 6.1 from Outotec Research Oy. To obtain the equilibrium composition of the reactions, minimization of Gibbs free energy was employed.

2.4. Membrane reactor set-up

Fig. 2(a) represents the scheme of the electrified-BSCF catalytic membrane reactor (e-CMR). In order to apply voltage to the capillary membrane, gold wires were connected at the end of the catalytic layer. To accurately control the membrane temperature (T_M), a thermocouple was attached to its surface, as indicated in Fig. 2(b). In contrast, an additional thermocouple was located in the middle of the reactor chamber (T_R), as shown in Fig. 2(a). For
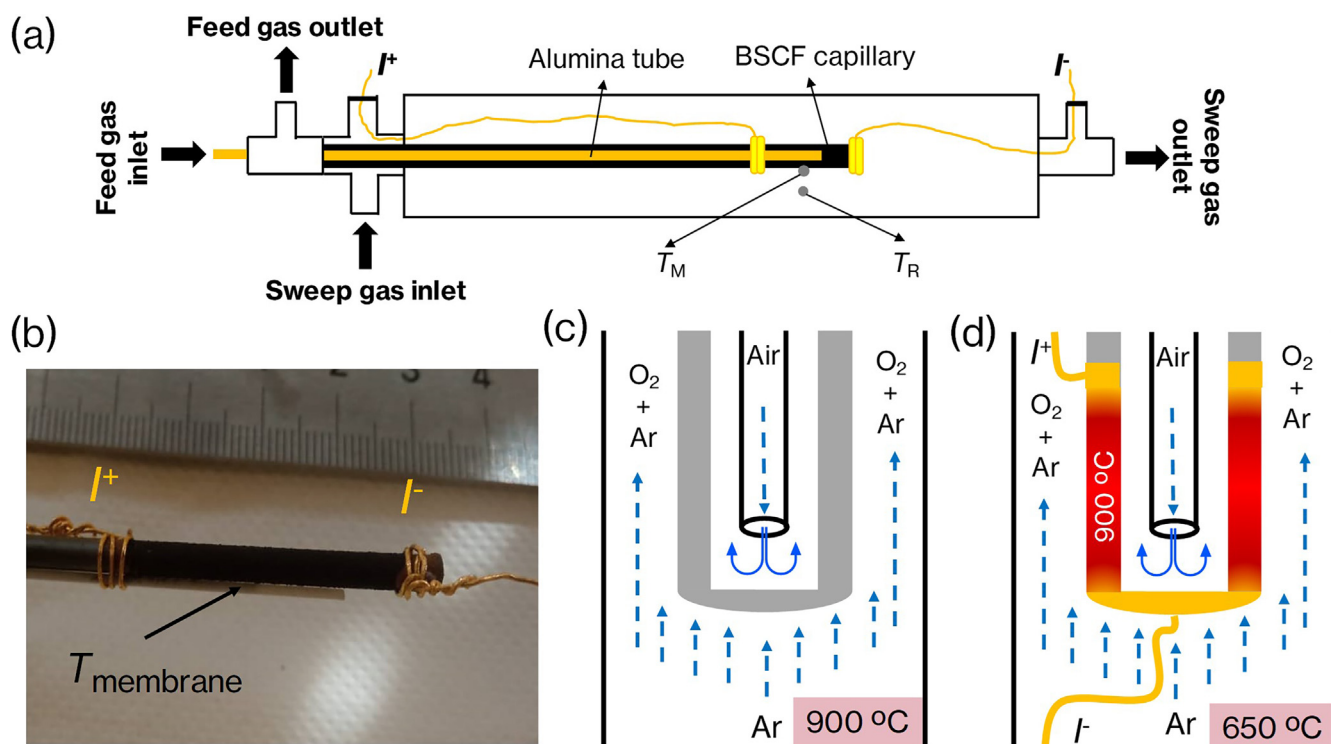

Fig. 2. (a) BSCF catalytic membrane reactor electrified device; (b) current gold wires connections and the temperature measurement of the membrane; (d) scheme of the non-electrified BSCF capillary membrane; (d) scheme of the Joule effect through the BSCF capillary membrane.

the non-electrified membrane, the oxygen permeation depends only on the reactor temperature (Fig. 2c). In the case of the electrified membrane, the application of voltage will produce local heating of the membrane, and the oxygen permeation will increase. With this technique, a maximum temperature of 900 °C on the membrane surface was obtained, whereas the reactor chamber was maintained at 650 °C (Fig. 2d).

For the oxygen permeation studies, the gas flow rate for both chambers, sweep (Ar) and feed (synthetic air), was 150 NmL min^{-1}. In the case of the ODHE reaction study, 400 NmL min^{-1} of a mixture of 10% ethane in Ar and 150 NmL min^{-1} of synthetic air were fed to the sweep and feed chamber, respectively. All the tests, permeation, and reaction were conducted at atmospheric pressure. In order to electrify, i.e., locally heat, the BSCF membrane, different electric voltages were applied for 60 min for both oxygen permeation and ODHE reaction experiments. Inlet gas streams were individually mass-flow controlled. The temperature was measured by two attached K-type thermocouples, one close to the membrane (T_M) and the other in the sweep chamber (T_R). Upon reaching the steady state, the permeation was analyzed by online gas chromatography (GC) using a micro-GC Varian CP-4900 equipped with Molsieve5A, Pora-Plot-Q glass capillary, and CP-Sil modules. Membrane gas leak-free conditions were ensured by continuously monitoring the N_2 concentration in the permeation gas stream (reaction chamber). Voltage was applied to the membranes by using a Keysight E36200 Series power supply. The Micro-GC was calibrated with a gas mixture of 11 compounds (Linde): 2% CH_4, 9% H_2, 9% CO, 1% CO_2, 1% C_2H_4, 2% C_2H_6, 1% C_3H_8, 1% C_3H_6, 1% C_3H_4, and 1% C_4H_6 in N_2. To calculate the conversion and the different selectivity obtained, the carbon balance was calculated.

$$2n_{C_2H_{6,in}} = 2\left(n_{C_2H_{6,out}} + n_{C_2H_4}\right) + n_{CO_2} + n_{CO} + 3(n_{C_3H_8} + n_{C_3H_6} + n_{C_3H_4}) + 4n_{C_{4+}} + n_{Coke} \tag{7}$$

Where n_{Ci} is the molar rate (mol min^{-1}) for each compound obtained at the outlet of the CMR. The initial ethane was measured by passing the catalytic membrane reactor, and coke formation was obtained from the carbon balance (Eq. (7)). Ethane conversion (X_{C2H6}), product selectivity (S_{Ci}), and ethylene yield (Y_{C2H4}) were calculated by using the Eqs. (8)–(10).

$$X_{C_2H_6} = \left(1 - \frac{2n_{C_2H_{6,out}}}{2n_{C_2H_{6,in}}}\right) \cdot 100 \tag{8}$$

$$S_{C_i} = \left(\frac{i \cdot n_{C_i}}{2\left(n_{C_2H_{6,in}} - n_{C_2H_{6,out}}\right)}\right) \cdot 100 \tag{9}$$

$$Y_{C_2H_4} = X_{C_2H_6} \cdot S_{C_2H_4}/100 \tag{10}$$

The oxygen permeation under ODHE reaction was calculated by using the hydrogen (Eq. (11)) and the oxygen balances (Eq. (12)). Water formation could be obtained from the hydrogen balance that, in addition, allows to get the oxygen balance and subsequently to calculate the oxygen permeation during the ODHE reaction.

Hydrogen balance

$$6n_{C_2H_{6,in}} = 6n_{C_2H_{6,out}} + 4n_{C_2H_4} + 8n_{C_3H_8} + 6n_{C_3H_6} + 4n_{C_3H_4} + 4n_{CH_4} + 6n_{C_4H_6} + 2n_{H_2} + 2n_{H_2O} \tag{11}$$

Oxygen balance

$$2n_{O_{2,perm}} = 2n_{O_{2,out}} + 2n_{CO_2} + n_{CO} + n_{H_2O} \tag{12}$$

3. Results and discussion

3.1. Microstructural study

The XRD analysis of BSCF capillary membranes (Fig. 3a) showed a single cubic perovskite phase; no secondary phases were detectable [42,43]. The microstructure of the catalytic layers was studied by SEM analysis of the cross-section. The BSCF catalytic layer has a thickness of around 20–30 μm and presents an adequate porosity, as shown in Fig. 3(b). The CTO catalytic layer presented a lower thickness, about 10–15 μm, and a lower particle size than the BSCF catalytic layer (Fig. 3c).

3.2. Influence of Joule effect on the oxygen permeation

First, the influence of the measurement configuration, sweep inside or outside the BSCF-activated capillary membrane, on the O_2 permeation flux was evaluated. 150 NmL min^{-1} of Ar and synthetic air were fed in the sweep and feed chamber. Fig. 4 shows the oxygen flux as a function of the temperature. At temperatures above 750 °C, lightly lower oxygen flows were obtained when the sweep was fed inside of the capillary, achieving 3.6 NmL min^{-1}-cm^{-2} at 900 °C whereas 3.9 NmL min^{-1} cm^{-2} was reached when the sweep side was fed in the outer chamber. These oxygen perme-
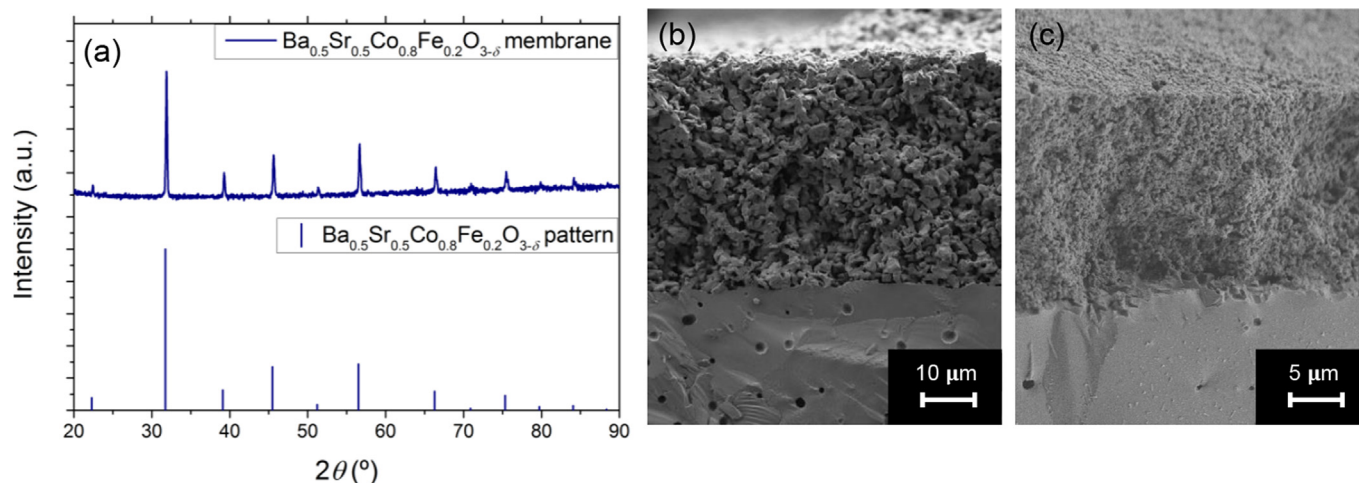

Fig. 3. (a) XRD patterns for the commercial BSCF capillary membrane, BSCF pattern from ICSD- I257399; cross-section SEM images of the BSCF membrane coated (b) with BSCF and (c) with CTO catalytic layers.
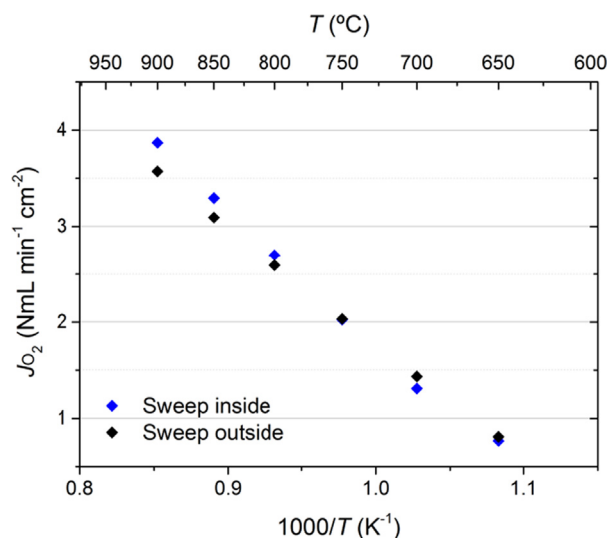
Fig. 4. Oxygen permeation through the surface-activated BSCF capillary membrane as a function of temperature for two different configurations of sweep fed inside (blue points) and outside (black points).

ation values were similar to other BSCF tubular membranes [44,45]. This behavior could be ascribed to the absence of a catalytic layer inside the membrane, as the surface exchange reactions on the sweep side are more affected than on the feed side [16,46]. At lower temperatures, the surface exchange reactions are not limiting, and both configurations present similar values [16,46].

The electrification of the system had been introduced using voltage pulses of 1 h (30 min at low voltage, from 1 to 5 V). After these peaks, the voltage was turned off in order to evaluate possible degradations. The results in Fig. 5(a) did not show degradation as a consequence of the electrification reaching the exact value of the oxygen permeation than before applying any potential. Further, the oxygen permeation and the temperature of the membrane increase gradually with the applied potential. Stable measurements could be observed when the potential is applied (both permeation and temperature). Fig. 5(b) compares the oxygen fluxes obtained in the conventional permeation test with the electrified measurement as a function of the reactor temperature. As voltage is applied to the membrane, it heats up, and the O_2 fluxes obtained are consistent with those obtained for the non-electrified permeation. Then, the temperature in the membrane was increased from 650 to 897 °C by applying 9 V (resulting in 33 W), reaching a flux of 3.7 NmL min^{-1} cm^{-2}. The same protocol was followed by changing the configuration, i.e., the sweep was fed in the inner chamber. In this configuration, the O_2 flux values (Fig. 5c) were lower than the corresponding non-electrified process for the same membrane temperature, reaching 3.2 NmL min^{-1} cm^{-2}. The power supply in both electrified configurations was compared in Fig. 5(d), giving rise to the same temperatures for both configurations. From this, it can be inferred that the gas configuration only affects the oxygen permeation values due to the position of the catalytic layer [16].

So far, the feasible voltage-driven control of the membrane-surface temperature and associated O_2 flux was demonstrated in the electrified mode. This BSCF electrified membrane reached 900 °C while the outer reaction chamber remained at 650 °C. In the following, the long-term stability of these electrified membranes under working conditions was assessed.

Evaluating the membrane robustness under electrified mode is especially relevant since the temperature gradient between membrane surface and the reactor chamber could cause thermomechanical stress and eventually break the membrane [47]. The

stability of the electrified membrane was studied by applying 9 V (3.7 A) for 110 h (Fig. 6). During the stability test, the temperature and current remained stable, resulting in a constant oxygen flux of 3.8 NmL min^{-1} cm^{-2} at 906 °C. After 110 h of operation, the application of voltage was stopped, leading to a decrease in both the voltage-induced membrane temperature and permeation flux. Namely, in the first measurement when the electric current was switched off, the oxygen flux was initially 1.2 NmL min^{-1} cm^{-2}, which, interestingly, is higher than the one reached in the previous experiments at the same temperature, around 0.76 NmL min^{-1} cm^{-2} (Table S1). From that point onwards, the oxygen permeation equilibrated until reaching a steady value of 0.55 NmL min^{-1} cm^{-2} after 40 h without voltage application. This effect could be related to the hexagonal phase formation in the BSCF structure [42,48,49]. The BSCF has two principal crystal perovskite structures, hexagonal (Space group $P6_3/mmc$) and cubic ($Pm\bar{3}m$) structures [48,49]. The BSCF with cubic structure presents superior transport properties than that with the hexagonal structure. The cubic structure is formed at 850–900 °C, but when the temperature decreases (i.e., when the electrical voltage is switched off), the hexagonal phase starts to grow [49]. Therefore, the oxygen flux drop was principally caused by the progressive formation of this hexagonal phase [49]. However, B-site doping with Y and Nb in BSCF can mitigate the formation of the hexagonal phase [50,51].

Despite the stable O_2 separation of the electrified BSCF-coated membrane when applying 3.7 A for 110 h, BSCF is not stable under CO_2 or reducing atmospheres such as CH_4. Therefore, applying protective layers under CO_2 environments, such as $Ce_{0.8}Gd_{0.2}O_{2-\delta}$ (CGO), to BSCF membranes can effectively mitigate the BSCF decomposition, as reported by Solis et al. [52]. In this work, a porous coating of $Ce_{0.8}Tb_{0.2}O_{2-\delta}$ (CTO) was selected to minimize the membrane degradation and increase the surface catalytic activity. This layer can also act as a catalytic layer due to the interesting electrochemical properties that the CTO possesses [53,54]. Then, the electrification of a BSCF capillary membrane functionalized with CTO was studied, and the main results are shown in Fig. 7 and Table S2.

Fig. 7(a) plots the oxygen permeation flux obtained with the membrane coated with CTO as a function of the reactor temperature for electrified and non-electrified modes. When the membrane is electrified, the voltage-induced membrane temperature increases and, subsequently, the oxygen flux. In this case, the reached maximum temperature in the membrane surface was 851 °C, and the corresponding oxygen flux was 3.8 NmL min^{-1} cm^{-2}, lower than the data obtained at 850 °C with the non-electrified membrane. CTO-coated membrane presents higher O_2 transport than BSCF-coated membrane when it is electrified, as observed in Fig. 7(b), where the oxygen flux is plotted as a function of the voltage-induced temperature. Notably, the reached heating power for the CTO-coated membrane is higher than that for the BSCF-coated membrane (Fig. S1), suggesting that higher local temperatures might be achieved in the BSCF bulk and the CTO catalytic porous layer presents better thermal insulation properties due to textural properties and the associated infrared radiation emissivity [55,56].

3.3. Oxidative dehydrogenation of ethane in BSCF catalytic membrane reactor

As mentioned above, the ODHE is a relevant chemical process for ethylene production that has gained considerable attention in the last few years [25,33]. Considering the thermodynamic equilibrium, the O_2/C_2H_6 ratio and the reaction temperature are crucial to boosting the ethylene selectivity and the ethane conversion. Fig. 8
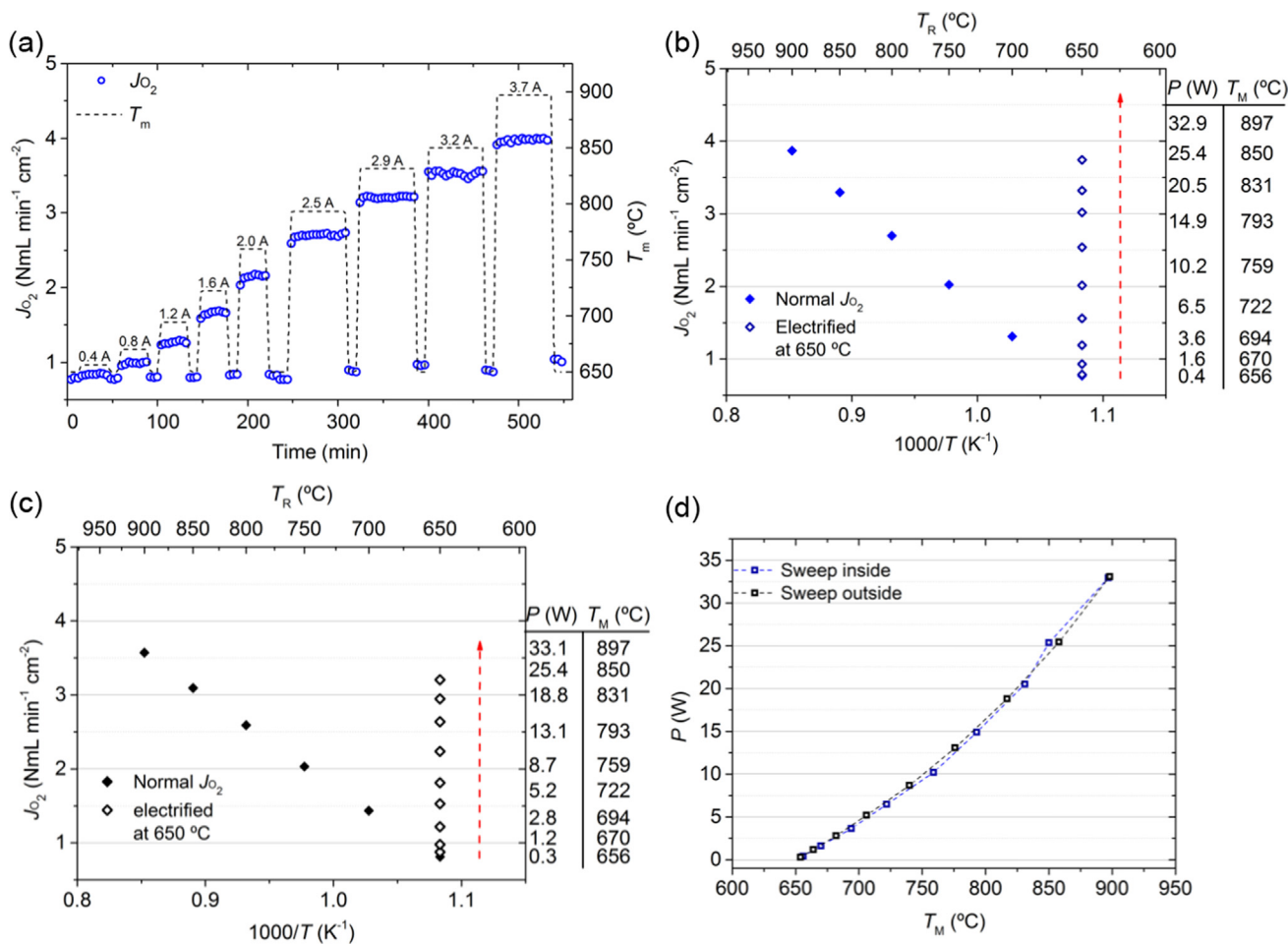
Fig. 5. Sweep outside configuration; (a) oxygen permeation and membrane temperature for different power applied at 650 °C; (b) oxygen permeation for an electrified and non-electrified BSCF membrane at different temperatures; Sweep inside configuration; (c) oxygen permeation for an electrified and non-electrified BSCF membrane at different temperatures; (d) power supply on the membrane and the membrane temperature reached for both configurations.
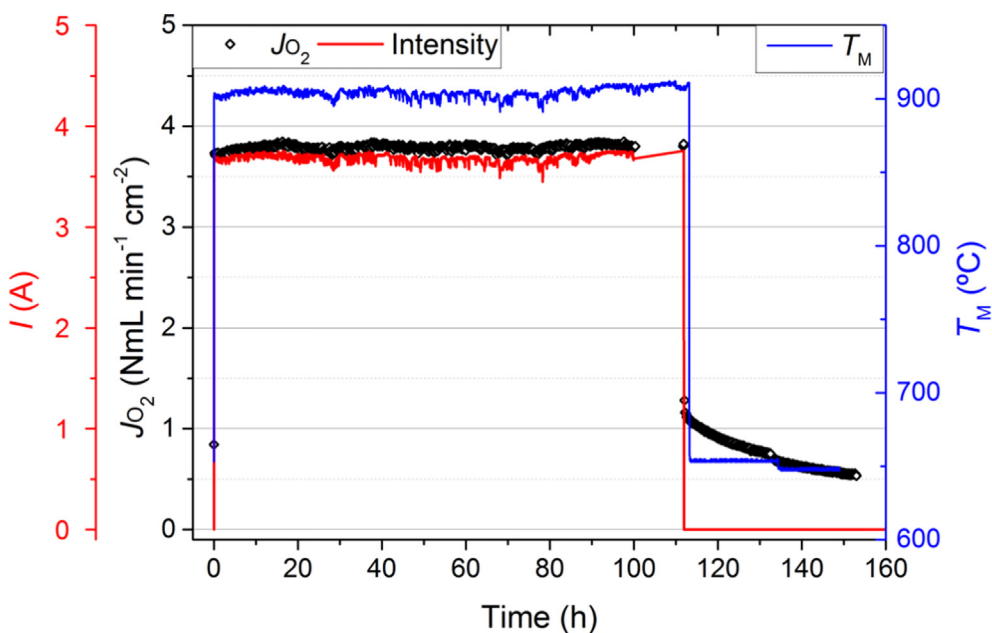

Fig. 6. Oxygen permeation stability test in electrification mode for 110 h.
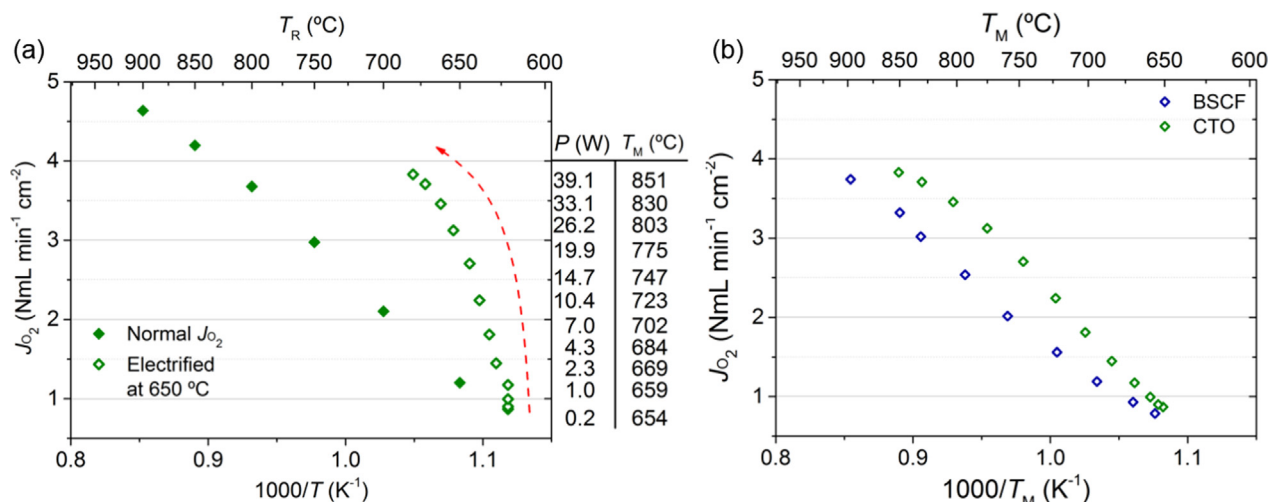
Fig. 7. (a) Oxygen permeation for an electrified and non-electrified BSCF membrane with CTO layer as a function of the reactor temperature; (b) comparison of the oxygen permeation obtained with BSCF and CTO-coated capillary membranes as a function of the membrane voltage-induced temperature when voltage is applied (sweep is fed in the outer chamber in both membranes).
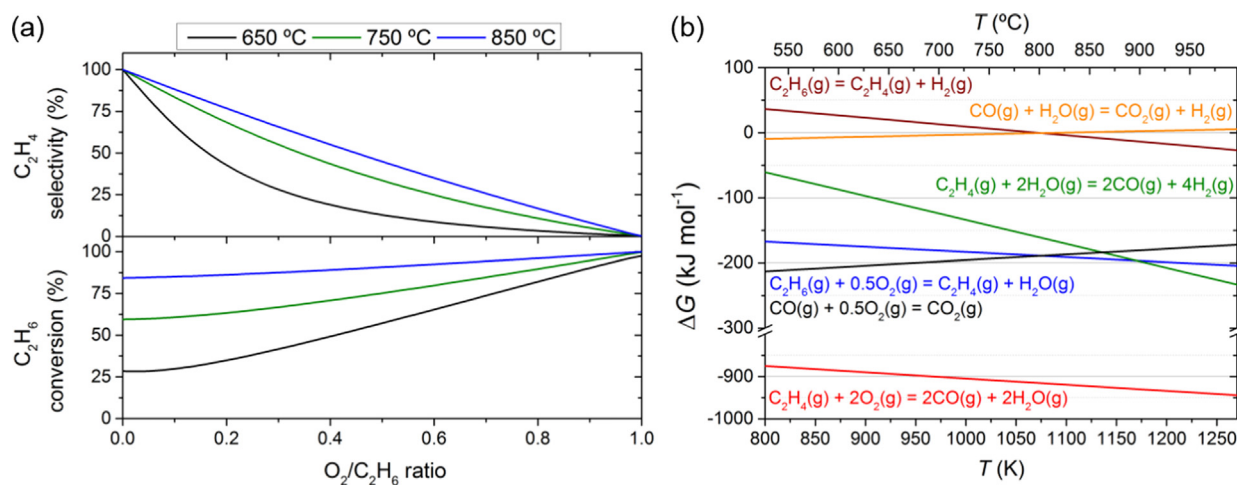

Fig. 8. (a) Ethane conversion and ethylene selectivity at the equilibrium at different O_2/C_2H_6 ratios at 650, 750, and 850 °C; (b) Gibbs free energy at different temperatures for the main reactions that can occur in the presence of O_2 and C_2H_6.

(a) shows the ethane conversion and ethylene selectivity at the thermodynamic equilibrium, and Fig. S2 shows the predicted product composition at different temperatures and O_2/C_2H_6 ratios. These thermodynamic calculations confirm that increasing the temperatures and lowering the O_2/C_2H_6 ratios increase ethylene production. Fig. 8(b) displays the Gibbs free energy as a function of the temperature for the different possible reactions in the ODHE reactor. Partial oxidation of ethylene has the most negative energy value, indicating that the partial oxidation contribution will become very relevant at high oxygen concentration. Also, the oxidation of CO is in the same order as the ODHE reaction, and steam reforming of ethylene also takes importance at high temperatures (>800 °C). To maximize ethylene yield, the O_2/C_2H_6 ratio has to be as low as possible, similar to pyrolysis conditions, limiting conventional catalytic ODHE technologies that use O_2 as a reactant to some extent. In this line, OTM emerges as a potential technology to improve the ODHE process [6,33–35].

ODHE reaction was performed using two different membranes and four different experiments were carried out. BSCF-coated membrane was heated at 650 °C (BSCF$_{650 °C}$) and 850 °C (BSCF$_{850}$

°C), respectively, and electrified BSCF- and CTO-coated membranes reached a temperature of ∼850 °C on the membrane surface while maintaining a temperature in the reactor chamber of 650 °C (BSCF$_{elect}$ and CTO$_{elect}$). Table 1 shows the conditions for these four experiments and the oxygen permeation when ethane is fed into the reaction chamber. Here, it also calculated the total ratio of O_2/C_2H_6 and the initial ratio of $\left(\frac{O_2}{C_2H_{6(in)}}\right)$, using the oxygen flux permeated and the 10% of the J_{O2} as the initial point of contact. The ethane feeding increases the oxygen-diffusion driving force between both chambers (lower P_{O2} than in Ar atmosphere), increasing the oxygen flux. The O_2 permeation results and the explanation of the behavior under the different conditions are given in Fig. S3.

The results for the ODHE reaction with the different evaluated membranes, electrified and non-electrified, are shown in Fig. 9. Fig. 9(a) plots the variation of the selectivity to ethylene as a function of the ethane conversion. In contrast, Fig. 9(b) shows the selectivity for all the reaction products generated during the catalytic test for the four performed experiments. The highest ethylene

Table 1
Oxygen permeation, reactor temperature, membrane temperature, and power supply for the different conditions in the ODHE test.

Experiment	T_R (°C)	T_M (°C)	Power supplied (W)	J_{O2} (NmL min^{-1} cm^{-2})	$\frac{O_2}{C_2H_6}$ [a]	$\frac{O_2}{C_2H_{6(in)}}$ [b]
BSCF$_{650\,°C}$	643	653	-	0.93 ± 0.08	0.07	2.4×10^{-3}
BSCF$_{elect}$	670	854	22.3	8.40 ± 0.06	0.65	2.2×10^{-2}
BSCF$_{850\,°C}$	856	877	-	10.6 ± 0.2	0.83	2.8×10^{-2}
CTO$_{elect}$	674	871	35.9	10.9 ± 0.1	0.88	2.7×10^{-2}

[a] $\frac{O_2}{C_2H_6} = \frac{J_{O2} \times Area}{F_{C2H6}}$

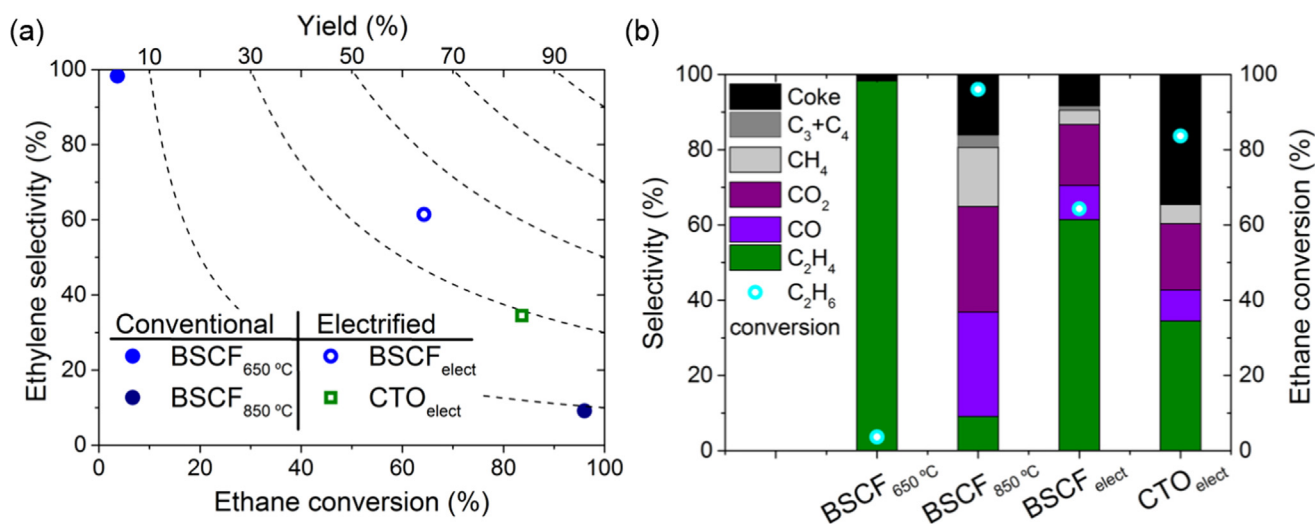[b] $\frac{O_2}{C_2H_{6(in)}} = \frac{J_{O2} \times 0.01}{F_{C2H6}}$

Fig. 9. (a) Ethylene selectivity as a function of ethane conversion for BSCF without electrification at different temperatures, 650 and 850 °C (BSCF$_{650\,°C}$ and BSFC$_{850\,°C}$) and for BSCF electrified at 850 °C (membrane temperature) with different catalytic layers, BSCF$_{elect}$ and CTO$_{elect}$; (b) product selectivity and ethane conversion for the different conditions of BSCF$_{650\,°C}$, BSCF$_{elect}$, BSFC$_{850\,°C}$, and CTO$_{elect}$.

selectivity was obtained for BSCF$_{650\,°C}$, whereas the obtained conversion is the lowest, corresponding to low O$_2$/C$_2$H$_6$ ratio and low reaction temperature (Fig. 8b and Table 1). On the opposite, BSCF$_{850\,°C}$ presents the highest ethane conversion and the lowest ethylene selectivity as predicted by the thermodynamic calculations at high reaction temperature and high O$_2$/C$_2$H$_6$ ratio (whereas an important selectivity to secondary products such as CO, CO$_2$, and CH$_4$ is observed). However, the ethylene yield obtained for both membranes did not reach more than 10%. Regarding the performance of the electrified experiments with both membranes, higher ethylene yields were obtained, reaching values of 30% and 40% for CTO$_{elect}$ and BSCF$_{elect}$, respectively. In the case of the electrified membranes, the production of CO$_2$, CO, and CH$_4$ was relevant in contrast with the corresponding selectivity observed at the BSCF$_{650\,°C}$, in which the ethylene selectivity is ∼100%. This difference in the selectivity was in line with the higher average O$_2$/C$_2$H$_6$ ratio (one order of magnitude higher) in the electrified membranes, while the nominal temperature in the outer reactor chamber remains similar for the three experiments. The superior catalytic performance of the electrified membrane reactors could be related to the combination of (1) the distributed oxygen dosing along the reaction coordinates and (2) the temperature gradient between the bulk gas stream (∼670 °C) and the catalytic membrane coating (850 °C), acting as ODHE catalyst and oxygen-delivery surface.

The O$_2$/C$_2$H$_6$ obtained in the electrified experiments was very similar to the BSCF$_{850\,°C}$, and the difference in the performance can not only be explained by the temperature difference. As oxygen permeation is distributed along the active membrane length, the O$_2$/C$_2$H$_6$ ratio progressively increases. Thus, to obtain a more accurate O$_2$/C$_2$H$_6$ ratio in the ODHE reaction, two different ratios

were calculated: (1) at the reactor inlet, taking into account the C$_2$H$_6$ fed in the reaction chamber (O$_2$/C$_2$H$_{6(in)}$) and (2) at the reactor outlet considering the C$_2$H$_6$ concentration (O$_2$/C$_2$H$_{6(out)}$) obtained in the GC analysis.

Fig. 10(a) plots both O$_2$/C$_2$H$_6$ ratios in the inlet and outlet of the reactor. In the outlet of the reactor, the obtained ratio for BSCF$_{850\,°C}$ was almost one order of magnitude higher than that for the electrified membranes, which could explain the better performance of the latter. Fig. 10(b) compares other ratios of interest in ODHE reaction for the different conditions, H$_2$/C$_2$H$_{6,\ reac}$ and H$_2$O/C$_2$H$_{6,\ reac}$. Both ratios indicate the extent of the partial oxidation of the ethylene, the thermal cracking of ethane, and steam reforming. In the case of BSCF$_{650\,°C}$, the H$_2$O/C$_2$H$_{6,\ reac}$ ratio was higher than 1, indicating that ODHE was not the main reaction taking place. Also, the presence of H$_2$ indicates that partial oxidation and water gas shift were produced. BSCF$_{850\,°C}$ reached the highest H$_2$/C$_2$H$_{6,\ reac}$, indicating that thermal cracking was produced. In the case of the electrified membranes, the BSCF$_{elect}$ shows a H$_2$O/C$_2$H$_{6,\ reac}$ ratio closer to 1, indicating that ODHE was the main reaction. Here, the presence of H$_2$, CO, and CO$_2$ suggests that other reactions, such as partial oxidation and water gas shift, occur. On the other hand, the CTO$_{elect}$ presents the highest H$_2$O/C$_2$H$_{6,\ reac}$ and O$_2$/C$_2$H$_{6,\ out}$ ratios, suggesting an essential contribution to the partial oxidation reaction.

In summary, Fig. 10(c) plots C$_2$H$_6$ conversion and C$_2$H$_4$ selectivity as a function of the O$_2$/C$_2$H$_6$ ratio in the outlet. C$_2$H$_6$ conversion increases with the O$_2$/C$_2$H$_6$ ratio and reactor temperature, whereas the opposite trend was observed for C$_2$H$_4$ selectivity in line with Fig. 9(a). The electrified membrane reactor enables it to reach conditions, i.e., temperature and O$_2$/C$_2$H$_6$ ratio, maximizing C$_2$H$_4$ yields.
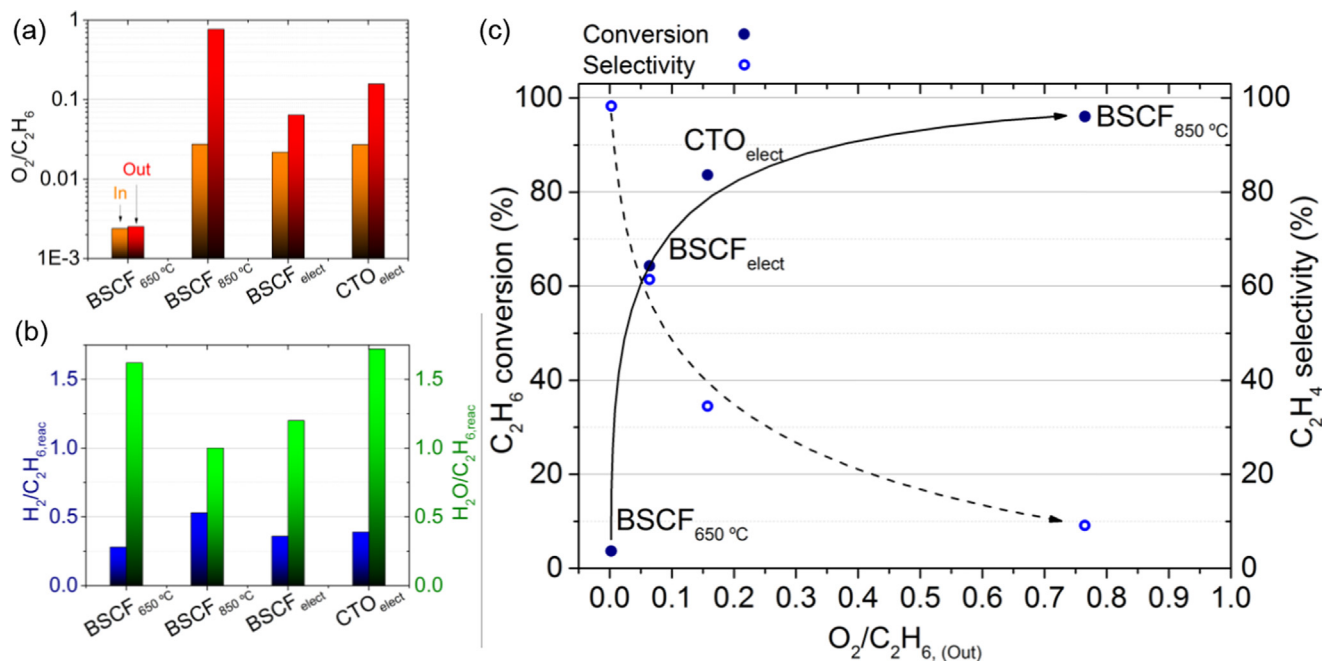
Fig. 10. (a) O_2/C_2H_6 ratio at the beginning and the end of the membrane for the different conditions in ODHE reaction; (b) $H_2/C_2H_{6,\ reac}$ and $H_2O/C_2H_{6,\ reac}$ for the different conditions in ODHE reaction; (c) C_2H_6 conversion and C_2H_4 selectivity at different O_2/C_2H_6 ratios at the end of the membrane for the different conditions.
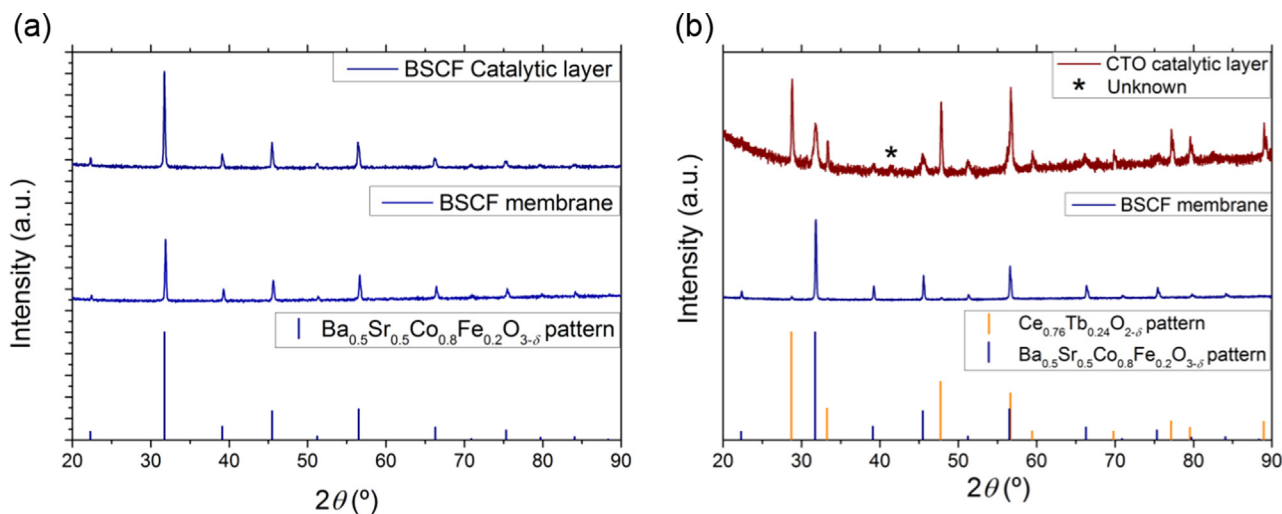

Fig. 11. XRD patterns after permeation and ODHE reaction tests of (a) BSCF catalytic layer and membrane and (b) CTO catalytic layer and BSCF membrane. ICSD codes: 193171 (CTO) and I257399 (BSCF).

3.4. Post-mortem characterization

Finally, the structural and microstructural stability of the different membranes was characterized after the oxygen permeation and the ODHE reaction tests. It should be mentioned that the BSCF membrane with the CTO catalytic layer was broken at the end of the experiment. On the other hand, the BSCF membrane with the BSCF catalytic layer was in perfect condition (Fig. S4a). The main difference between both membranes was the power supplied to achieve 850 °C on the membrane surface. Namely, 22.3 and 35.9 W is supplied for the BSFC-coated membrane and CTO-coated membrane, respectively.

XRD measurements of the spent catalytic layer and the bulk membranes were performed separately by scratching the catalytic layer and measuring it and, then grinding part of the membrane after removing the catalytic layer. In the case of the BSCF membrane with a BSCF catalytic layer, no secondary phases or impurities are detected in Fig. 11(a). For the CTO-coated membrane, the presence of a minor secondary phase was detected, which might be attributed to the BSCF hexagonal phase according to literature (Fig. 11b) [57,58]. Some minor quantities of CTO remain in the BSCF membrane after scratching the catalytic layer, as observed in Fig. 11(b).

The microstructure of the membranes was studied by SEM. Some particle sintering and agglomeration of the catalytic layer are observed in the BSCF-coated membrane (Fig. 12a and b). In addition, within the occluded pores (Fig. 12c and d), some filamentous morphology may correspond to the BSCF hexagonal phase
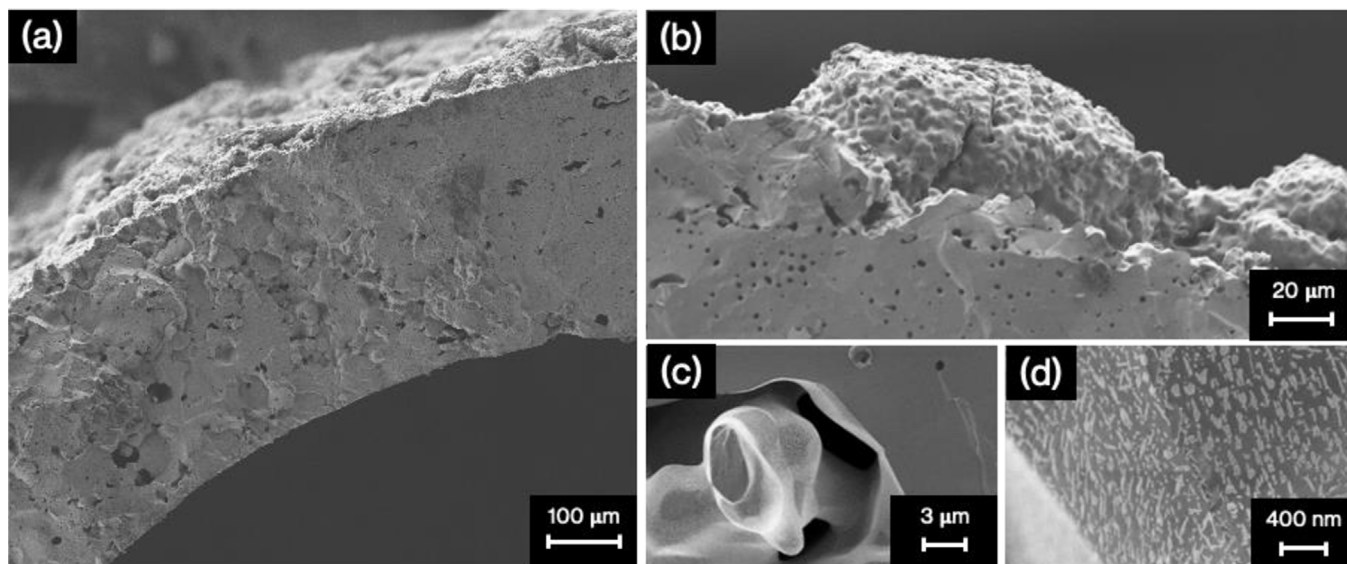
Fig. 12. Cross-section SEM image for the BSCF capillary membrane after electrification and ODHE reaction. (a) Membrane and catalytic layer; (b) BSCF catalytic layer; (c) occluded pore inside the bulk of the BSCF membrane; (d) magnification of the occluded pore surface.

that appears at temperatures below 900 °C [59,60]. The formation of this secondary phase is related to the lowering of the oxygen permeation at 650 °C after electrification in the oxygen permeation stability test.

In the case of the CTO-coated membrane, densification and detachment of the catalytic layer are observed (Fig. 13a and b) and could explain the lower permeation obtained under electrified conditions. The observed delamination could also be attributed to the different thermal expansion coefficient (TEC) of the catalytic CTO layer and the BSCF membrane, 11.4 and 16–20 × 10⁻⁶ K⁻¹, respectively [61,62]. The electrification for this membrane likely

led to higher temperatures in the BSFC bulk, leading to more extensive sintering in the catalytic layers. Also, in this case, this secondary phase was present within the occluded porosity and throughout the membrane bulk (Fig. 13c and d). This secondary phase is similar to the CoO phase, indicating that the membrane temperature was locally close to 1000 °C [59,60]. These impurities could be formed when the membrane collapsed during the ODHE reactions (Fig. S4b). Two different phases can be observed in the CTO layer (Fig. 13e and f) related to the high-temperature cobalt diffusion, also observed by XRD.
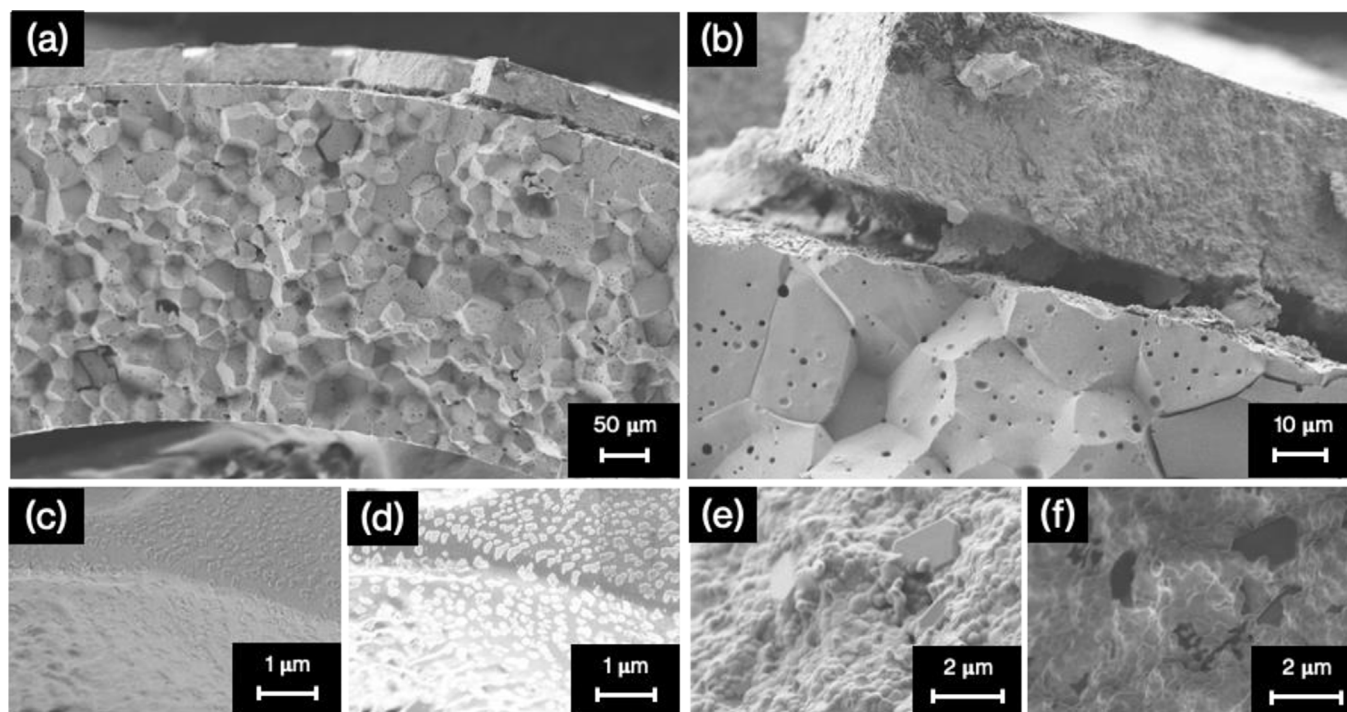

Fig. 13. Cross-section SEM image for the CTO capillary membrane after electrification and ODHE reaction. (a) Membrane and catalytic layer; (b) CTO catalytic layer; (c) BSCF membrane bulk with SE2 detector; (d) BSCF membrane bulk with InLens detector; (e) CTO catalytic layer with SE2 detector; (f) CTO catalytic layer with InLens detector.

4. Conclusions

The electrification of a $Ba_{0.5}Sr_{0.5}Co_{0.8}Fe_{0.2}O_{3-\delta}$-based oxygen-transport membrane enabled the in-situ heating via the Joule effect. This method facilitates (1) the membrane temperature control independent of the temperature of the surrounding bulk gas stream and (2) the control of the oxygen flux through the membrane. For a capillary membrane coated with a porous BSCF catalytic layer, 900 °C was achieved on the membrane surface while the outer reactor chamber remained at 650 °C by applying a current along the capillary and reaching an electric power of 33 W. Moreover, the membrane under electrified mode showed very stable oxygen permeation flux for >100 h.

The electrification effect was studied on a membrane coated with $Ce_{0.8}Tb_{0.2}O_{2-\delta}$ (CTO), acting as a protective barrier and catalytic layer. In this case, the protective layer also affects the reached thermal regime, reaching a lower temperature on the membrane surface, i.e., 850 °C instead of 900 °C, for the same current applied (3.7 A). This membrane was more affected by the diffusion limitations during the permeation test, obtaining a different oxygen permeation when the sweep gas was increased from 150 to 400 NmL min^{-1}, rising from 3.7 to 5.2 NmL min^{-1} cm^{-2}, respectively. This effect was explained by that the sintering of the catalytic layer decreased the surface-exchange reaction rate.

The electrified membrane reactors showed superior ODHE catalytic performance. The ethylene yield was 4-fold improved through the BSCF-membrane electrification, i.e., from 10% to ~40%. In electrified conditions, the selectivity to secondary reactions was significantly reduced compared to ODHE at 850 °C (conventional heating). Differentiated O_2/C_2H_6 ratios during the ODHE reaction could be reached via electrification, reaching balanced O_2/C_2H_6 ratios to mitigate partial oxidation reactions, preserving the ethylene selectivity. The electrified membrane reactors effectively combine (1) the distributed oxygen dosing along the reaction coordinates and (2) the temperature gradient between the bulk gas stream (~670 °C) and the catalytic membrane coating (850 °C), acting as ODHE catalyst and oxygen-delivery surface. Electrified oxygen transport membranes hold great potential for ODHE reactors due to the adjustable thermal regime and the control of the O_2/C_2H_6 ratios. This reactor concept can be applied to membrane processes, opening new avenues for electrification of the chemical industry.

Declaration of competing interest

The authors declare that they have no known competing financial interests or personal relationships that could have appeared to influence the work reported in this paper.

Acknowledgments

Appendix A. Supplementary data

Supplementary data to this article can be found online at https://doi.org/10.1016/j.jechem.2023.12.008.

References

[1] Y.H. Kim, S.K. Min, N.P. Gillett, D. Notz, E. Malinina, Nat. Commun. 14 (2023).
[2] M. Harmsen, C. Tabak, L. Höglund-Isaksson, F. Humpenöder, P. Purohit, D. van Vuuren, Nat. Commun. 14 (2023).
[3] L. Chen, S.Z. Yong, A.F. Ghoniem, Prog. Energy Combust. Sci. 38 (2012) 156–214.
[4] A. Arratibel Plazaola, A. Cruellas Labella, Y. Liu, N. Badiola Porras, D. Pacheco Tanaka, M. Sint Annaland, F. Gallucci, Processes 7 (2019) 128.
[5] Y. Dai, X. Gao, Q. Wang, X. Wan, C. Zhou, Y. Yang, Chem. Soc. Rev. 50 (2021) 5590–5630.
[6] R.C. Schucker, G. Dimitrakopoulos, K. Derrickson, K.K. Kopeć, F. Alahmadi, J.R. Johnson, L. Shao, A.F. Ghoniem, Ind. Eng. Chem. Res. 58 (2019) 7989–7997.
[7] V.R. Choudhary, S.A.R. Mulla, V.H. Rane, J. Chem. Tech. Biotech. 71 (1998) 167–172.
[8] N. Nauels, S. Herzog, M. Modigell, C. Broeckmann, J. Memb. Sci. 574 (2019) 252–261.
[9] F. Wu, M.D. Argyle, P.A. Dellenback, M. Fan, Prog. Energy Combust. Sci. 67 (2018) 188–205.
[10] N.F. Himma, A.K. Wardani, N. Prasetya, P.T.P. Aryanti, I.G. Wenten, Rev. Chem. Eng. 35 (2019) 591–625.
[11] R.J. Allam, Energy Proc. 1 (2009) 461–470.
[12] J. Sunarso, S.S. Hashim, N. Zhu, W. Zhou, Prog. Energy Combust. Sci. 61 (2017) 57–77.
[13] A. Giuffrida, P. Chiesa, F. Drago, L. Mastropasqua, in: Energy Procedia, Elsevier Ltd, 2018, pp. 599–606.
[14] A.C. Bose, Inorganic Membranes for Energy and Environmental Applications, Springer, New York, New York, NY, 2009.
[15] M.G. Sahini, B.S. Mwankemwa, N. Kanas, Ceram. Int. 48 (2022) 2948–2964.
[16] D. Catalán-Martínez, A. Santafé-Moros, J.M. Gozálvez-Zafrilla, J. García-Fayos, J. M. Serra, Chem. Eng. J. 387 (2020) 124069.
[17] S. Baumann, J.M. Serra, M.P. Lobera, S. Escolástico, F. Schulze-Küppers, W.A. Meulenberg, J. Memb. Sci. 377 (2011) 198–205.
[18] Q. Jiang, K.J. Nordheden, S.M. Stagg-Williams, J. Memb. Sci. 369 (2011) 174–181.
[19] W.K. Hong, G.M. Choi, J. Memb. Sci. 346 (2010) 353–360.
[20] H. Wang, Y. Cong, W. Yang, Catal. Today 82 (2003) 157–166.
[21] H. Wang, Y. Cong, W. Yang, Catal. Today 104 (2005) 160–167.
[22] J. Garcia-Fayos, M.P. Lobera, M. Balaguer, J.M. Serra, Front. Mater. 5 (2018) 31.
[23] C.E. Beall, E. Fabbri, A.H. Clark, N.S. Yüzbasi, T. Graule, T.J. Schmidt, EcoMat (2023) e12353.
[24] Z. Cao, H. Jiang, H. Luo, S. Baumann, W.A. Meulenberg, H. Voss, J. Caro, Catal. Today 193 (2012) 2–7.
[25] D. Fairuzov, I. Gerzeliev, A. Maximov, E. Naranov, Catalysts 11 (2021) 833.
[26] Y. Gao, L. Neal, D. Ding, W. Wu, C. Baroi, A.M. Gaffney, F. Li, ACS Catal 9 (2019) 8592–8621.
[27] S. Lei, A. Wang, G. Weng, Y. Wu, J. Xue, H. Wang, J. Energy Chem. 77 (2023) 359–368.
[28] Y. Fan, X. Xi, D. Medvedev, Q. Wang, J. Li, J.L. Luo, X.Z. Fu, J. Power Sources 515 (2021) 100133.
[29] W. Wu, H. Hu, D. Ding, Cell Rep. Phys. Sci. 2 (2021) 100405.
[30] G. Luongo, F. Donat, A.H. Bork, E. Willinger, A. Landuyt, C.R. Müller, Adv. Energy Mater. 12 (2022) 2200405.
[31] S. Yusuf, L.M. Neal, F. Li, ACS Catal. 7 (2017) 5163–5173.
[32] M. Hurtado Cotillo, D. Unsihuay, C.E. Santolalla-Vargas, A. Paredes Doig, R. Sun Kou, G. Picasso, Catal. Today 356 (2020) 312–321.
[33] S. Najari, S. Saeidi, P. Concepcion, D.D. Dionysiou, S.K. Bhargava, A.F. Lee, K. Wilson, Chem. Soc. Rev. 50 (2021) 4564–4605.
[34] Z. Stansch, L. Mleczko, M. Baerns, Comprehensive Kinetics of Oxidative Coupling of Methane over the La_2O_3/CaO Catalyst, Ind Eng Chem Res 36 (1997) 2568–2579.
[35] Y. Gao, F. Haeri, F. He, F. Li, ACS Catal. 8 (2018) 1757–1766.
[36] M.P. Lobera, S. Valero, J.M. Serra, S. Escolástico, E. Argente, V. Botti, Chem. Eng. Sci. 66 (2011) 6308–6317.
[37] M.P. Lobera, M. Balaguer, J. Garcia-Fayos, J.M. Serra, ChemCatChem 4 (2012) 2102–2111.
[38] M.P. Lobera, S. Escolástico, J.M. Serra, ChemCatChem 3 (2011) 1503–1508.
[39] D. Chen, Z. Shao, Int. J. Hydrogen Energy 36 (2011) 6948–6956.
[40] W. Araki, Y. Takemura, Y. Arai, J. Malzbender, J. Electrochem. Soc. 161 (2014) F3001–F3004.
[41] H. Zhao, W. Shen, Z. Zhu, X. Li, Z. Wang, J. Power Sources 182 (2008) 503–509.
[42] F. Wang, T. Nakamura, K. Yashiro, J. Mizusaki, K. Amezawa, Phys. Chem. Chem. Phys. 16 (2014) 7307–7314.
[43] P. Müller, H. Störmer, L. Dieterle, C. Niedrig, E. Ivers-Tiffée, D. Gerthsen, Solid State Ionics 206 (2012) 57–66.

[44] P. Haworth, S. Smart, J. Glasscock, J.C. Diniz da Costa, Sep. Purif. Technol. 94 (2012) 16–22.
[45] S. Liu, G.R. Gavalas, J. Memb. Sci. 246 (2005) 103–108.
[46] J.H. Joo, K.S. Yun, J.-H. Kim, Y. Lee, C.-Y. Yoo, J.H. Yu, A.C.S. Appl, Mater. Interfaces 7 (2015) 14699–14707.
[47] S. Herzog, C. Liu, N. Nauels, A. Kaletsch, C. Broeckmann, Membranes (Basel) 12 (2022) 1093.
[48] D.N. Mueller, R.A. de Souza, T.E. Weirich, D. Roehrens, J. Mayer, M. Martin, Phys. Chem. Chem. Phys. 12 (2010) 10320–10328.
[49] C. Niedrig, S. Taufall, M. Burriel, W. Menesklou, S.F. Wagner, S. Baumann, E. Ivers-Tiffée, Solid State Ionics 197 (2011) 25–31.
[50] M. Meffert, L.S. Unger, H. Störmer, F. Sigloch, S.F. Wagner, E. Ivers-Tiffée, D. Gerthsen, J. Am. Ceramic Soc. 102 (2019) 4929–4942.
[51] V. Weber, M. Meffert, S. Wagner, H. Störmer, L.S. Unger, E. Ivers-Tiffée, D. Gerthsen, J. Mater. Sci. 55 (2020) 947–966.
[52] C. Solís, M. Balaguer, J. Garcia-Fayos, E. Palafox, J.M. Serra, Sustain, Energy Fuels 4 (2020) 3747–3752.
[53] M. Laqdiem, J. Garcia-Fayos, L. Almar, M. Balaguer, J.M. Serra, J. Membr. Sci. (2023) 121578.
[54] M. Balaguer, C. Solís, J.M. Serra, Chem. Mater. 23 (2011) 2333–2343.
[55] L. Wang, G. Xu, C. Liu, H. Hou, S. Tan, Surf. Coat. Technol. 357 (2019) 559–566.
[56] X. Zhao, C. Liu, C. Xu, G. Xu, Y. Zhang, S. Tan, Y. Han, Infrared Phys. Technol. 92 (2018) 454–458.
[57] S. Švarcová, K. Wiik, J. Tolchard, H.J.M. Bouwmeester, T. Grande, Solid State Ionics 178 (2008) 1787–1791.
[58] C. Niedrig, Electrochemical Performance and Stability of $Ba_{0.5}Sr_{0.5}Co_{0.8}Fe_{0.2}O_{3-\delta}$ for Oxygen Transport Membranes, KIT Scientific Publishing, Karlsruhe, 2015.
[59] P. Müller, H. Störmer, M. Meffert, L. Dieterle, C. Niedrig, S.F. Wagner, E. Ivers-Tiffée, D. Gerthsen, Chem. Mater. 25 (2013) 564–573.
[60] D. Gerthsen, M. Meffert, H. Störmer, V. Wilde, L. Almar, F. Sigloch, L.-S. Unger, S. F. Wagner, E. Ivers-Tiffée, ECS Trans. 77 (2017) 35–39.
[61] P. Shuk, M. Greenblatt, M. Croft, Chem. Mater. 11 (1999) 473–479.
[62] M. Brisotto, F. Cernuschi, F. Drago, C. Lenardi, P. Rosa, C. Meneghini, M. Merlini, C. Rinaldi, J. Eur. Ceram. Soc. 36 (2016) 1679–1690.